Journal of Geophysical Research: Space Physics

RESEARCH ARTICLE
10.1029/2017JA025077

Horseshoes in the High-Latitude Ionosphere

Ningchao Wang[1], Seebany Datta-Barua[1], Alex T. Chartier[2], Uriel Ramirez[1], and Cathryn N. Mitchell[3]

[1]Mechanical, Materials, and Aerospace Engineering, Illinois Institute of Technology, Chicago, IL, USA, [2]Johns Hopkins University Applied Physics Laboratory, Laurel, MD, USA, [3]Department of Electronic and Electrical Engineering, University of Bath, Bath, UK

Key Points:
- Lagrangian coherent structures (LCSs) are found in two-dimensional modeled plasma drifts of the high latitude ionosphere
- Forward time LCSs have a "U," or horseshoe, pattern oriented to open on the nightside and respond to geomagnetic activity by shifting equatorward
- Independent observations confirm that patches originate from plasma that is poleward of the dayside LCS boundary

Supporting Information:
- Supporting Information S1
- Movie S1

Correspondence to:
N. Wang,
nwang20@hawk.iit.edu

Citation:
Wang, N., Datta-Barua, S., Chartier, A. T., Ramirez, U., & Mitchell, C. N. (2018). Horseshoes in the high-latitude ionosphere. *Journal of Geophysical Research: Space Physics*, *123*, 5831–5849. https://doi.org/10.1029/2017JA025077

Received 4 DEC 2017
Accepted 7 JUN 2018
Accepted article online 19 JUN 2018
Published online 20 JUL 2018

Abstract In the high-latitude ionosphere, predicting transport of polar cap patches is important because of their impact on radio communications and navigation systems. Lagrangian coherent structures (LCSs) are barriers to transport in nonlinear time-varying flow fields, found by computing the local maximum finite-time Lyapunov exponent (FTLE). We propose that LCSs are barriers governing patch formation. In this work, we compute and visualize the LCSs in high-latitude ionospheric convection by computing the FTLE field with the Ionosphere-Thermosphere Algorithm for Lagrangian Coherent Structures (ITALCS). The Weimer 2005 high-latitude electric potential model and the 12th-generation International Geomagnetic Reference Field (IGRF-12) are used to generate the $\vec{E} \times \vec{B}$ drift field at each gridpoint in the ionosphere. The $\vec{E} \times \vec{B}$ drifts are used as the input to ITALCS. Time-varying structures are detected in two-dimensional ionospheric drifts at high latitudes based on locally maximum forward time FTLE values for both geomagnetically stormy and quiet periods. Typically, the dominant structure is shaped like the letter "U," or a "horseshoe," oriented with the curved portion of the "U" on the dayside around local noon. The LCSs during the geomagnetically stormy period have more complex topology and shift equatorward compared to the LCSs during quiet times. Analysis of a polar cap patch observed on 17 March 2015 with the Multi-Instrument Data Analysis System indicates that a necessary condition for its formation and transport is that storm enhanced density exist poleward of the LCS.

1. Introduction

In the high-latitude upper atmosphere poleward of the auroral oval, the polar cap patch is a few 100-km-scale ionospheric enhancement surrounded by lower-density plasma (Crowley, 1996). A polar cap patch is often associated with ionospheric plasma density irregularities varying from 100 m to several kilometers scale size that adversely affect Global Navigation Satellite System (GNSS) service (Moen et al., 2013) by causing scintillation, a rapid fluctuation in signal amplitude and phase (Datta-Barua et al., 2015; Zhang, Zhang, Lockwood, et al., 2013; Zhang, Zhang, Moen, et al., 2013). The mechanism for scintillation is electromagnetic wave scattering due to variations in density (Sotnikov et al., 2014). Polar cap patch scintillations are believed to arise due to a number of possible instability mechanisms (Atul et al., 2018; Burston et al., 2016; Moen et al., 2013).

While there is no consensus on how exactly patches lead to scintillation, Moen et al. (2013) points out the importance of tracking patches and the flow channels and shears in which they drift, which can drive instabilities. For this reason, sensing patches and their movement has become an important application of ionospheric tomographic and assimilative algorithms (Bust & Crowley, 2007). By using plasma density and path-integrated total electron content (TEC) measurements, ionospheric imaging can produce electron density in two, three, and four dimensions including temporal variation, as reviewed by Bust and Mitchell (2008).

Polar cap patch movement is coupled to the magnetosphere. In the high latitudes, magnetospheric field lines transition from the closed lines that return to Earth in the opposite hemisphere to open lines that extend into interplanetary space and may interconnect with the interplanetary magnetic field (IMF; Hunsucker & Hargreaves, 2003). The polar cap describes the ionospheric region of open field lines that are swept back away from the sun. The cusps are the regions on the dayside in both hemispheres in which the magnetic field lines extend to the dayside magnetopause, the boundary between the IMF and magnetosphere.

Due to solar wind motion, magnetospheric flux tubes typically circulate from noon to midnight across the polar cap, with return circulation around the dawn and dusk sides. Superposed with a corotation electric field,

this circulation maps down along the field lines into the ionosphere to form what is typically a two-cell electric potential pattern (Hunsucker & Hargreaves, 2003). This cross-polar-cap electric field combined with the magnetic field largely governs plasma motion at high latitudes. During geomagnetic storms, magnetic reconnection is a framework for understanding the erosion of the dayside magnetopause. Enhanced erosion of the flux on the dayside leads to an accumulation on the nightside (Carlson, 2012). Observation and theory both show that geomagnetic storms are enhanced when the IMF points southward ($B_z < 0$); magnetic reconnection is especially effective in this condition.

After initiating on the dayside cusp region, patches are transported across the center of the polar cap region toward night side (Moen et al., 2015; Oksavik et al., 2010) and may circulate back on the dawn and dusk sides. Of the unresolved questions regarding polar cap patches, in this work we focus on asking the following: What is the source of the plasma? Formation mechanisms of polar cap patches were studied by Lockwood and Carlson (1992); Lockwood et al. (2005); MacDougall and Jayachandran (2007); Weber et al. (1984); and Zhang et al. (2011) and classified as Type L for low-density patches ionized by particle precipitation and Type H for high-density ones formed by segmenting the (TOI; Zhang, Zhang, Moen, et al., 2013). In this work we focus on the H-type patches. A backward tracing of a polar cap patch studied by Bust and Crowley (2007) indicates that the patch did not originate from the midlatitude part of the TOI. TOIs themselves are observed to form from midlatitude storm enhanced density (SED), which has been defined as a latitudinally narrow, spatially continuous region of enhanced plasma density extending from geomagnetic midlatitude (Foster, 1993). A subauroral polarization stream (SAPS) has been theorized as an electric field mechanism in the dusk sector for erosion of SED into a TOI (Foster et al., 2005).

Zhang, Zhang, Moen, et al. (2013) refers to patches as caused by an equatorward shift of the open-closed field line boundary "entraining" ionized plasma into the polar cap. Moen et al. (2015) notes that regional forecasts of scintillation conditions require an understanding of how plasma is "entrained" into the polar cap convection flow, as well as its exit. Hosokawa et al. (2009) and Hosokawa, Tsugawa, et al. (2010) describe GPS TEC-based observations originally reported by Foster et al. (2005) of a TOI "entrained" into the noontime cusp and into the nightside along a streamline.

Hosokawa, St-Maurice, et al. (2010) note that "time varying plasma flow is an important factor for producing patches." However, in a time-varying flow, streamlines differ from pathlines, the actual trajectories of individual fluid elements. For this reason, a TOI structure does not always align with instantaneous electric isopotentials, which are effectively streamlines (e.g., Foster et al., 2005; Zhang, Zhang, Lockwood, et al., 2013; Zou et al., 2014).

Fluid coherent structures are features of a time-evolving flow that persist in space and time. Coherent structures indicate transport and energy transfer processes. A formal definition of coherence in Earth's fluid environment can be challenging (Venditti et al., 2013) particularly for turbulent and time-varying fluid flows, such as that of the ionosphere. Yet analyzing coherent structures can help in forecasting the transport of plasma patches, mitigating their impacts on transionospheric signals. Many approaches for identifying flow coherence have relied on Eulerian definitions of structures such as vorticity, but these definitions are not observer independent (Haller, 2005), so they are inappropriate to study in Earth's noninertial frame at global scale (Wang et al., 2017).

For this reason, we analyze the high-latitude plasma drift flow in the Lagrangian frame that moves with the fluid, to find Lagrangian coherent structures (LCSs). LCS analysis is a numerical method in fluid dynamics to predict transport and interaction processes (Haller, 2015; Shadden et al., 2005). LCSs are frame-invariant manifolds indicating ridges of maximum divergence or convergence in a time-varying nonlinear flow. LCSs act as barriers to material transport, demarcating regions of qualitatively different flow patterns.

One analogy to help make the distinction in what we mean by a "fluid coherent structure" would be to consider a hurricane: The clouds are the material that are visible, akin to the polar cap patch itself. However, within the flow field there may exist a flow structure (e.g., the vortex), whether or not clouds are there. Whereas Eulerian definitions of the vortex would help define the eye of the hurricane, the LCS serves to define the perimeter of the hurricane (du Toit & Marsden, 2010).

LCSs have had wide application in geophysical transport phenomena. The spread of contaminants in the Earth's fluid environment such as oil spills on the sea surface and airborne volcano ash can be predicted via the LCS technique (Peacock & Haller, 2013). The work by du Toit and Marsden (2010), to which this paper's

title alludes, showed that horseshoe-shaped LCSs described hurricane entrainment in the troposphere. Thermospheric LCSs were found as material transport barriers that respond to geomagnetic activity (Wang et al., 2017). LCSs have also been found in stellar plasmas (BozorgMagham et al., 2013). Previous study of LCSs in ionospheric plasma solved fluid mass and ion and electron momentum equations for midlatitude E and F region over a 100-km-scale horizontal region (Tang & Mahalov, 2013).

However, to treat patches requires a larger scale flow domain, in which the plasma fluid is regarded as a single species. In this work, we analyze synoptic scale ionospheric LCSs, specifically asking: Are there governing structures in the high-latitude ionosphere? Do the structures guide and predict possible patch formation or transport sites? For this analysis, the flow of interest is the plasma drift convection as a flow field at high latitudes in both hemispheres. While in general plasma drift is a superposition of electric Pedersen drift, gravitational Pedersen drift, pure gravitational drift, and parallel mean flow (Atul et al., 2018; Sotnikov et al., 2014), in the high-latitude region above 50° geomagnetic latitude, the plasma drift is dominated by $\vec{E} \times \vec{B}$ drift due to the absence of vertical shears (Anderson et al., 1996a; Kirchengast, 1996). The $\vec{E} \times \vec{B}$ drift is governed by the local electric and magnetic fields:

$$\vec{v}_{E\times B} = \frac{-\vec{\nabla} V \times \vec{B}}{B^2} \tag{1}$$

where V is an electrostatic potential function and $\vec{B}$ is the magnetic field. At high latitudes, this $\vec{E} \times \vec{B}$ drift is primarily horizontal and is understood to describe magnetic flux tube transport. For simplification, we treated the high-latitude plasma drift as the $\vec{E} \times \vec{B}$ drift. Such an assumption has also been used in several ionospheric models such as Global Theoretical Ionospheric Model, which has been used to model polar patches of enhanced F-region plasma density (Decker et al., 1994; Sojka et al., 1993) and boundary blobs (Anderson et al., 1996b).

We show the anticipated global high-latitude ionospheric LCSs based on two-dimensional flows computed by modeled electric field and magnetic field. We show that (1) LCSs exist in the ionosphere; (2) they respond to geomagnetic activity by shifting equatorward; and (3) LCSs can give insight into necessary conditions for the formation and transport of the H-type polar cap patch; namely, that the TOI must exist poleward of the LCS in order for patches to be possible and that they are guided along LCS channels afterwards. We do this by simulating ionospheric convection with modeled electric and magnetic fields during a geomagnetically quiet period and an active period. We use data-driven observations of a polar cap patch that are confirmed with an independent data set. We examine this polar cap patch's relationship with the modeled ionospheric LCSs over time. This paper is organized as follows: we summarize our algorithm to identify the ionospheric LCSs in section 2 with details provided in Appendices A and B; in section 3, we describe the method we use in determining whether ionospheric LCSs exist, whether they respond to geomagnetic activity, and the LCS relationship to polar cap patches; then we show results in section 4, broader implications in section 5, and a summary in section 6.

2. Ionosphere-Thermosphere Algorithm for LCSs

In this work, we apply the finite-time Lyapunov exponent (FTLE) technique to define the ionospheric LCSs. The ridge (or surface in a three-dimensional flow) of maximal FTLE values represents a barrier in material transport (Shadden et al., 2005). The basic equations may be found in numerous resources (Grigoriev, 2011; Haller, 2015) and are summarized here for a two-dimensional flow domain. Advection of the fluid particle at each point $x = (x^1, x^2)$ at time t can be described as

$$\dot{x} = v(x,t), \;\; x \in U, t \in [t_0, t_f] \tag{2}$$

where $U \subset \mathbb{R}^2$ is the domain. A flow map maps particles at all initial positions x_0 at t_0 to their current positions $x(t_f; x_0, t_0)$ at final time t_f after a finite period of time $\tau = t_f - t_0$:

$$F_{t_0}^{t_f}(x_0) = x(t_f; x_0, t_0)\,, \; t \in [t_0, t_f] \tag{3}$$

$$= x_0 + \int_{t_0}^{t_f} v(x,t)dt \tag{4}$$

where $x_0 = x(t_0; x_0, t_0)$, and the velocity v is integrated to propagate fluid elements forward in time.

The flow map traces a fluid particle from initial position x_0 to a final position after time τ. By keeping track of each particle's initial and final positions, we may quantify the amount of stretching that has occurred by computing the Jacobian of the flow map. For each particle in a two-dimensional flow domain this is a 2×2 matrix:

$$\mathbf{J} \equiv \nabla F_{t_0}^{t_f}(x_0) = \begin{bmatrix} \frac{x^1(t_f;t_0,x_0^1+\delta^1)-x^1(t_f;t_0,x_0^1-\delta^1)}{|2\delta^1|} & \frac{x^1(t_f;t_0,x_0^1+\delta^1)-x^1(t_f;t_0,x_0^1-\delta^1)}{|2\delta^2|} \\ \frac{x^2(t_f;t_0,x_0^2+\delta^2)-x^2(t_f;t_0,x_0^2-\delta^2)}{|2\delta^1|} & \frac{x^2(t_f;t_0,x_0^2+\delta^2)-x^2(t_f;t_0,x_0^2-\delta^2)}{|2\delta^2|} \end{bmatrix} \tag{5}$$

where δ^1, δ^2 are infinitesimal displacements in each respective direction of the domain. Then the FTLE σ at t_0 is the normalized maximum eigenvalue λ_{max} of the Cauchy-Green Deformation Tensor $\mathbf{J}^T\mathbf{J}$ as follows:

$$\sigma(\mathbf{J}) = \frac{1}{|\tau|} \log\left(\sqrt{\lambda_{max}\left(\mathbf{J}^T\mathbf{J}\right)}\right) \tag{6}$$

An FTLE is computed for every initial particle x_0 in the domain, and the LCS is the ridge of local FTLE maxima, a maximally repelling material surface. To find LCSs of maximum attraction, the integration in equation (4) may be carried out backwards in time. In this work we examine forward-time FTLEs only.

Based on the equations above, we developed the Ionosphere-Thermosphere Algorithm for LCSs (ITALCS) to investigate upper atmospheric LCSs. ITALCS uses input 2-D velocity data to compute the FTLE scalar fields as well as tracer trajectories. The spatial domain for which ITALCS computes FTLE values and tracer trajectories must be discretized into a regular mesh of generalized coordinates, specified by bounds on x^1, x^2 and resolutions δ^1, δ^2 for each. The temporal domain $[t_0, t_f]$ defines the time interval within which ITALCS may compute the integration shown in equation (4). Within that time interval, velocity fields must be provided over the grid at $n+1$ epochs spaced in time by Δt such that $\tau = n\Delta t$.

For the forward-time FTLE computation, after reading in the input velocities for the gridded domain and timespan specified, ITALCS computes the FTLE values for every initial gridpoint in the domain. We use the particles' positions at a chosen start time t_0 to find the particles' ending positions by numerically integrating over duration τ. The velocity data are provided at time intervals Δt, which is subdivided into m smaller intervals dt with $\Delta t = mdt$. In this way the flow map in equation (4) is discretized as

$$x(t_f; x_0, t_0) \approx x_0 + \sum_{i=0}^{n-1} v_i(x_i, t_i)\Delta t \tag{7}$$

$$\approx x_0 + \sum_{i=0}^{n-1}\sum_{j=0}^{m-1} v_i(x_{ij}, t_{ij})dt \tag{8}$$

The purpose of the subdivision $\Delta t = mdt$ is to decouple the integration interval and accuracy of the results from the velocity field data cadence. If velocity field data are provided by measurement, the Δt resolution may be limited by the measurement process. In the case of a model, as in this study, having $\Delta t > dt$ decreases runtime of the model significantly. After each numerical integration step dt, since the particle at $x(t_{ij}; x_0, t_0)$ will not in general fall at exactly another gridpoint, the velocity data are bilinearly interpolated to its location. The flow map computation starts at t_0 and stops at t_f after integration time τ. The Jacobian matrix is composed by substituting a particle's starting position $x(t_0; x_0, t_0)$ and ending position $x(t_f; x_0, t_0)$ into equation (5). The output FTLE scalar field from equation (6) for a given t_0 is a matrix of the same dimension as the meshed grid domain. For tracer trajectory calculations, ITALCS outputs the intermediate locations $x(t_0 + i\Delta t; x_0, t_0)$ and final position $x(t_f; x_0, t_0)$ of a tracer particle. To demonstrate how ITALCS works we tested a canonical flow, the time-varying 2-D double gyre, given in the literature (Shadden et al., 2005). The location and shape of the LCS and the FTLE values in Appendix A are identical to those shown by Shadden et al. (2005).

To identify the LCS in a spherical domain such as the ionosphere, we search globally to ensure a closed domain. For a given altitude, we mesh the domain for the generalized coordinates $x^1 = \phi, x^2 = \lambda$ where ϕ and λ are geographic longitude and latitude, respectively. Figure 1 is the workflow for using ITALCS to compute the final position $\vec{r}^P$ at time t_f and associated FTLE σ of a particle P in a flow initialized at a gridpoint (ϕ_0, λ_0). A particle P's velocity ${}^E\vec{v}^P$ in an Earth-fixed frame (indicated by the "E" presuperscript), is output from a velocity model for a given $\vec{r}^P$. This velocity (v_e, v_n) is expressed in east-north coordinates local to each point, and transformed

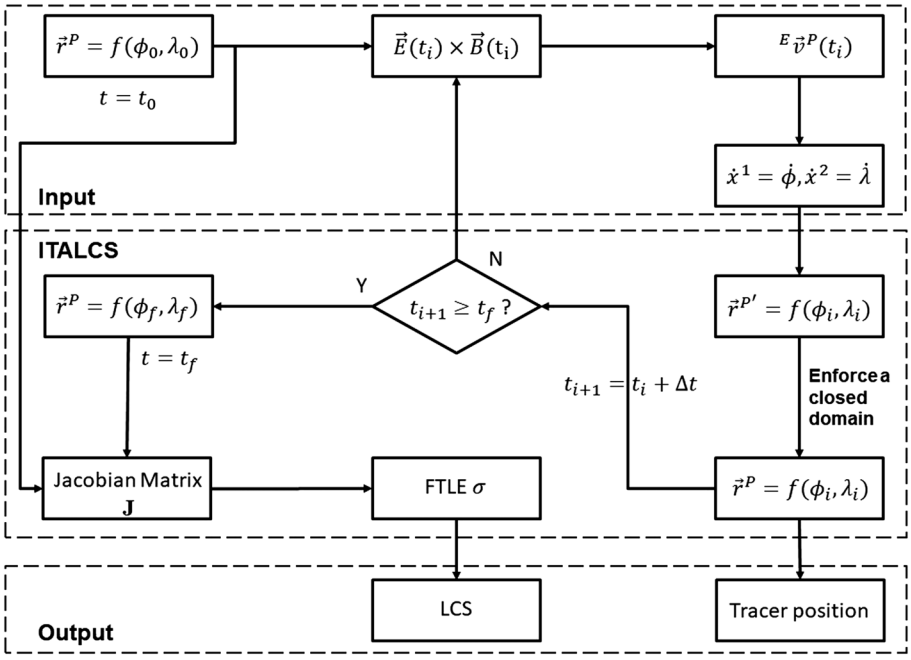

Figure 1. Process for tracing the horizontal position of particle *P* in Earth's ionosphere over time and computing the finite-time Lyapunov exponent to identify the Lagrangian coherent structures in the flow.

to angular rates $\dot{\phi}, \dot{\lambda}$ as described in Appendix B. ITALCS updates the coordinates of the particle according to equation (8) to be (ϕ_i, λ_i) at time $t_{i+1} = t_i + \Delta t$, wrapping the longitude and latitude back into the domain $\phi = [-180°, 180°], \lambda = [-90°, 90°]$ if needed, as described in Appendix B. At the next epoch, the velocity field is generated at the gridpoints with the velocity model and bilinearly interpolated to the particle's current location (ϕ_i, λ_i). Tracing the particle until time t_f gives the final position (ϕ_f, λ_f) of particle *P*, after which the FTLE can be computed with equation (6). Repeating this process for every initial gridpoint in the domain we generate the FTLEs for the whole domain as output as well as individual tracer locations if desired.

3. Method

In this work, we test (1) whether LCSs exist at high latitude of the modeled plasma drifts, (2) whether the high latitude ionospheric LCSs respond to geomagnetic activity, and (3) what the LCS indicates about the polar cap patch source plasma region. To do this, we compute the high latitude plasma drifts with the electric potential simulated with Weimer 2005 and magnetic field modeled by the 12th generation International Geomagnetic Reference Field (IGRF-12; Thébault et al., 2015) and provide them as the input to ITALCS to get the FTLE scalar fields. The Weimer 2005 polar electric potential model is used for generating the global potential *V*, and IGRF-12 is used for simulating the global magnetic field $\vec{B}$. Then the $\vec{E}\times\vec{B}$ drift field at each gridpoint *P* in a single layer of the ionosphere is computed by applying the outputs of those two models to equation (1) and taking the horizontal zonal and meridional components to obtain (v_e, v_n), which is used as *v* in equation (2).

$$ {}^E\vec{v}^P = \underbrace{(\vec{v}_{E\times B} \cdot \hat{l}_2)}_{v_e}\hat{l}_2 + \underbrace{(\vec{v}_{E\times B} \cdot \hat{l}_3)}_{v_n}\hat{l}_3 = v_i(x_i, t_i) \tag{9} $$

where the coordinates are as shown in Figure B1. The velocity ${}^E\vec{v}^P$ is ground speed v_e and v_n (in m/s) at a geodetic location (ϕ, λ) for a given altitude and time. While the $\vec{E} \times \vec{B}$ drift by definition lies in the 2-D plane normal to the local $\vec{B}$ field at every point, at high latitudes at which the $\vec{B}$ field is nearly vertical, the $\vec{E} \times \vec{B}$ drift is primarily horizontal. Therefore, treating the 2-D convection as horizontal flow in this work $\vec{v}_{E\times B} \approx^E \vec{v}^P$ is a reasonable approximation for high latitudes.

Since Weimer 2005 is a high-latitude model we search for 2-D ionospheric LCSs in the high latitude zone. However, we simulate the flow field at global scale to avoid discontinuity at the middle-to-high-latitude boundary. The 2-D global domain is parameterized with longitude and latitude as the generalized coordinates

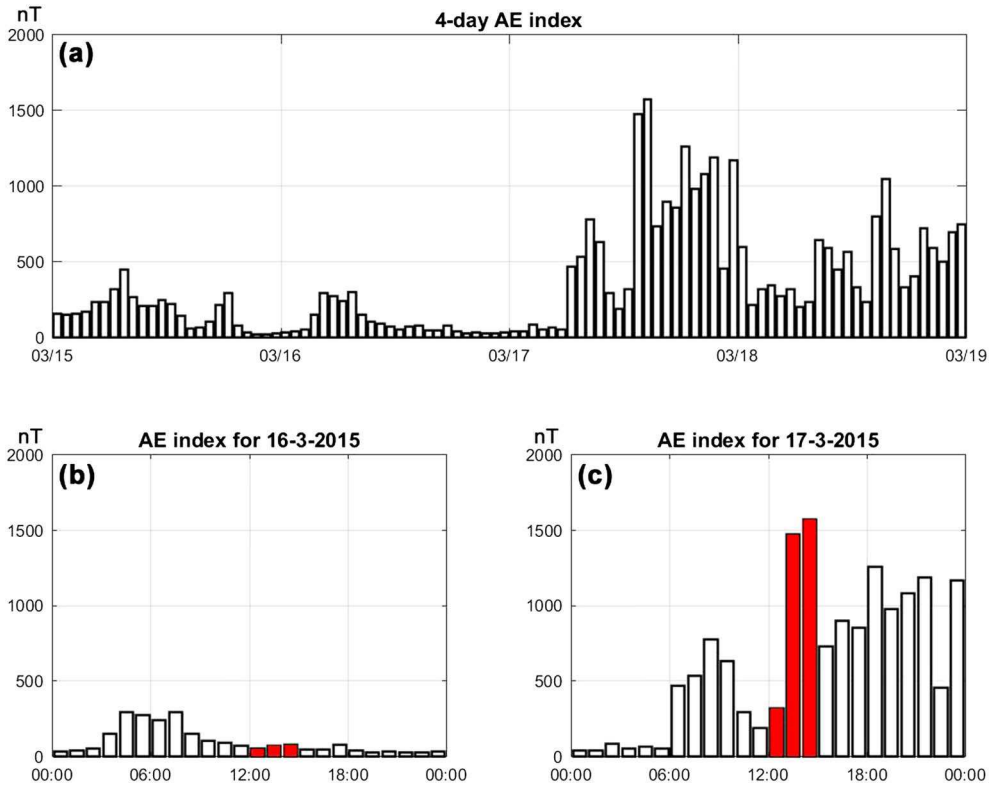

Figure 2. (a) AE index from 15–18 March 2015; (b) AE index for geomagnetic quiet period on 16 March 2015; (c) AE index for geomagnetic period on 17 March 2015. The periods labeled in red in (b) and (c) are used to study the influence of geomagnetic activity.

with a 1° resolution in each direction. In the domain, each gridpoint is assumed to contain a particle at time t_0. The plasma drifts for these particles are computed every $\Delta t = 5$ min, with $dt = 30$ s. Due to the fact that plasma drift velocities are large (~1,000 m/s) at high latitudes, we choose $\tau = 3$ hr as the integration time.

For the first and second studies we simulated the $\vec{E} \times \vec{B}$ drift at 350˜km height. We use the AE index to select a geomagnetically quiet period and a geomagnetically stormy period. AE is defined by the separation between the indices AU and AL of the upper and lower envelopes of auroral-zone magnetic observation (Kamide & Rostoker, 2004).

Figure 2a plots the AE index for 15–18 March 2015. For the first study, in which we examine whether LCSs exist in the convection field, we choose four periods with initial time t_0 as 00:00 UT, 06:00 UT, 12:00 UT, and 18:00 UT (see Figure 2b)

For the second study, to explore the influence of geomagnetic activity on the ionospheric LCSs, we select $t_0 =$ 12:00 UT on 16 March 2015 as the initial time of the geomagnetically quiet period and $t_0 =$ 12:00 UT on 17 March 2015 for the geomagnetically active period. The AE index for these 2 days are shown in Figures 2b and 2c, respectively. Choosing the two periods within 2 days ensures similar dipole tilt angle and solar cycle conditions. IMF measurements during the storm can be found in Le et al. (2016). We also set up three tracers at high latitudes for both the geomagnetically quiet period with $t_0 =$ 12:00 UT 16 March 2015, and storm period with $t_0 =$ 12:00 UT 17 March 2015. The three tracers are initially equally spaced in latitude on the local noon longitude, with A_0 at 76°N, B_0 at 72°N, and C_0 at 68°N for the quiet period and A_0 at 66°N, B_0 at 62°N, and C_0 at 58°N for the active period. Their corresponding final positions are A_f, B_f, and C_f. The tracer locations are chosen to demonstrate the effect of LCSs lying between the particles. We also compare LCSs to electric potential contours.

For the last study, we identify a polar cap patch at 16:40 UT on 17 March 2015 based on observational data. We simulate the ionospheric conditions on 17 March 2015 at 450 km before and after, tracing the polar cap

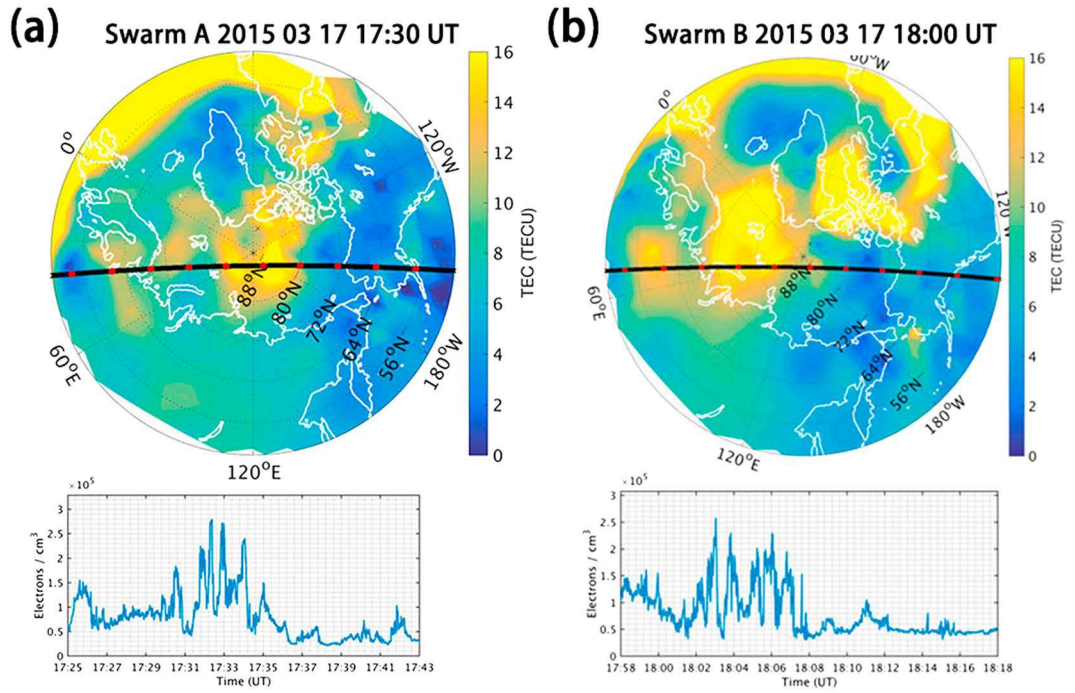

Figure 3. (Top) MIDAS reconstructed vertical TEC maps over the geographic north pole at (a) 17:30 UT and (b) 18:00 UT. The Swarm satellite track is marked in black. Swarm travels from left to right across the plot. Regular time intervals are marked with red dots. (Bottom) Swarm satellite in situ densities measured over time for the satellite track shown. MIDAS = Multi-Instrument Data Analysis System; TEC = total electron content.

patch at 16:40 UT forward in time for 100 min to study its transport, backward in time for 60 min to study its formation, and identifying the associated dominant LCS during those times based on the modeled drifts.

The patch is observed in TEC maps of the ionosphere generated using Multi-Instrument Data Analysis System (MIDAS). MIDAS performs three-dimensional, time-dependent electron density inversions constrained by vertical basis functions based on Chapman profiles and horizontal Tikhonov regularization (Chartier et al., 2012; Mitchell & Spencer, 2003; Spencer & Mitchell, 2007). About 100 high-latitude dual-frequency GPS reference stations from the International GNSS Service network are used in the inversion, which are performed at 10-min resolution from 00:00 to 24:00 UT for 17 March 2015.

To show that the MIDAS results are reconstructing patches of enhanced plasma, Figure 3 shows the MIDAS estimates of polar cap patches with geographic north pole TEC maps at (a) 17:30 UT and (b) 18:00 UT. These are compared with in situ measurements of Swarm satellite densities at about 450-km altitude over time, as the satellites pass through the vicinity of the patches at those times. In these plots, a point on the satellite ground track on the map corresponds to the instant on the density time series subplot directly below it. The correspondence of high and low densities with high and low TEC regions spatially gives strong evidence that the TEC estimated by MIDAS in fact corresponds to polar cap patch plasma.

4. Results

Figure 4 shows world maps of FTLE values at 350 km viewed from the geographic north pole for 16 March 2015 at (a) t_0 = 00:00 UT, (b) t_0 = 06:00 UT, (c) t_0 = 12:00 UT, and (d) t_0 = 18:00 UT. In each map, closely spaced contour lines represent the FTLE values from 0 to 5×10^{-4}. Since LCSs are located at local FTLE maxima, the absolute value of the FTLE is not significant. The blank area at lower latitudes is due to the vanishing of the Weimer potential to 0. On these maps, a bright yellow ridge is a repelling LCS. Horseshoe-like ridges appear in the day sector oriented with the "U" opening on the local nightside at around 70° latitude. There are secondary structures poleward of the main horseshoe, but these appear to vary with initial time t_0. The fact that the horseshoe opens on the nightside indicates that there is not a strong flow repulsion on that side.

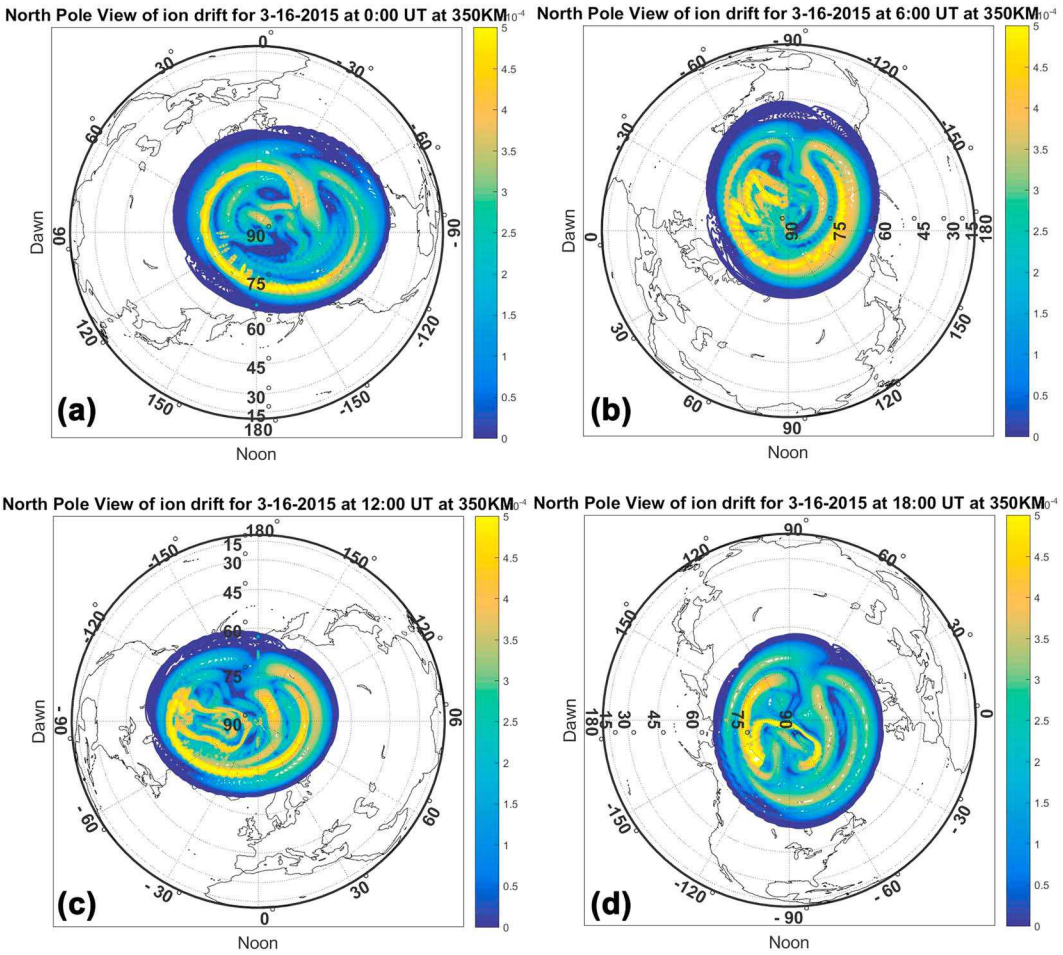

Figure 4. FTLE map for plasma drifts at 350 km viewed from the geographic north pole for 16 March 2015 at (a) t_0 = 00:00 UT; (b) t_0 = 06:00 UT; (c) t_0 = 12:00 UT; and (d) t_0 = 18:00 UT, each with integration time τ = 3 hr. Local noon is fixed at the bottom of each figure. The color scale represents the FTLE values varying from 0 to 5×10^{-4}; yellow ridges are the LCSs. FTLE = finite-time Lyapunov exponent; LCS = Lagrangian coherent structure.

To study the effect of geomagnetic activity on ionospheric LCSs, we use t_0 = 12:00 UT as the initial time for both geomagnetic quiet and active periods. Figures 5a and 5b show the FTLE maps over the northern and southern poles for the geomagnetically quiet period at t_0 = 12:00 UT 16 March 2015, and Figures 5c and 5d show the FTLE maps over both poles for the geomagnetically active period at t_0 = 12:00 UT 17 March 2015. In Figure 5a tracers are initialized in the northern hemisphere on the local noon longitude with A_0 at 76°N, B_0 at 72°N, and C_0 at 68°N, and in Figure 5c tracers are initialized with A_0 at 66°N, B_0 at 62°N, and C_0 at 58°N. The trajectories of the three tracers are shown in Figures 5a and 5c with the final positions labeled A_f, B_f, and C_f.

The motion of the tracers shown in Figure 5a indicate that over 3 hr, particle A has a change in position $(\Delta\phi, \Delta\lambda)$ = (123.7°E, 2°N). In contrast, B has $(\Delta\phi, \Delta\lambda)$ = (39.6°W, 3.5°S), and particle C shifts by $(\Delta\phi, \Delta\lambda)$ = (0.6°W, 0°N) from its initial position. There is a local maximum FTLE structure between A_0 and B_0 indicating a repelling LCS. With equal separations at the initial positions of the three tracers, the final distance $\overline{A_f B_f}$ is larger than $\overline{B_f C_f}$, which corresponds to the FTLE values between them.

Compared to the results of the geomagnetically quiet period, the storm time LCSs in Figures 5c and 5d are more complex and appear at lower latitudes for both hemispheres. During 3 hr, tracer A shown in Figure 5c has a change in position $(\Delta\phi, \Delta\lambda)$ = (70.2°E, 1.5°S), and B has $(\Delta\phi, \Delta\lambda)$ = (126.4°E, 4.3°N). In contrast, particle C shifts by $(\Delta\phi, \Delta\lambda)$ = (43.5°W, 4.6°S) from its initial position. The larger separation tendency between B and C than B and A corresponds to the larger FTLE value between B_0 and C_0. Figure 5c shows that LCSs run east-west in the local day sector at 60°N and curve poleward at the local night sector. Figures 5b and 5d show maps of LCSs over the geographic south pole for the quiet and active periods, respectively. Similar structuring

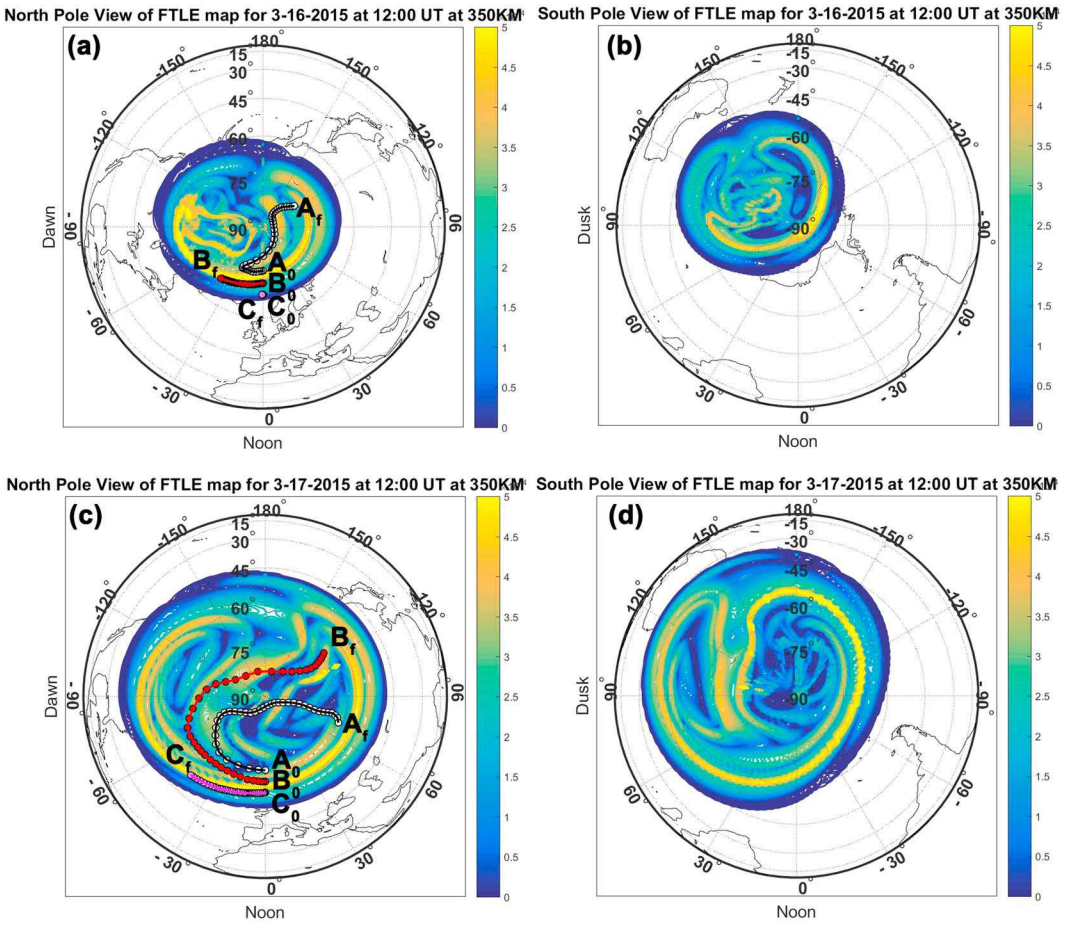

Figure 5. Finite-time Lyapunov exponent maps of plasma drifts at 350 km over the northern and southern hemispheres. The color scale in each map represents the FTLE values ranging from 0 to 5×10^{-4}. In the northern hemisphere, tracers' initial and final positions are labeled as A_0 and A_f (white), B_0 and B_f (red), and C_0 and C_f (magenta). (a) North pole, geomagnetically quiet period at t_0 = 12:00 UT, 16 March 2015, τ = 3 hr. (b) South pole, geomagnetically quiet. (c) North pole, geomagnetically active period at t_0 = 12:00 UT, 17 March 2015, τ = 3 hr. (d) South pole, geomagnetically active.

and response to geomagnetic activity is observed. The LCSs do not appear to have perfect conjugacy between northern and southern high latitudes.

The LCS structures are reminiscent of the two-cell potential and convection pattern modeled by Weimer 2005. For this reason we compare the LCS locations to electric potential contours. Figure 6 contains the north pole view plots of LCS ridges superimposed over electric potential contours simulated by Weimer 2005 for the geomagnetically quiet period (Figure 6a), and geomagnetically active period (Figure 6b). In Figures 6a and 6b, the red ovals are the electric potential boundary over the full time interval τ which is the equatormost point of vanishing potential during the interval $t = [t_0, t_f]$. The purple ridges are the repelling LCSs identified as $\sigma \geq 2.5{\times}10^{-4}$. Comparing Figures 6a and 6b, it is clear the electric potential boundary for the geomagnetically active period is lower in latitude than the boundary for the geomagnetic quiet period, so the LCSs for the geomagnetically active period appear more equatorward than the LCSs for geomagnetic quiet period. The color contour lines are the electric potential modeled by Weimer 2005 at time t_0. For both storm and quiet periods, the most equatorward LCS ridges in the day sector are parallel to the electric potential boundary.

In order to explore the formation and propagation of the polar cap patch, we apply the LCS analysis technique to the flows at 16:40 UT on 17 March 2015, at which time, a polar cap patch is visually identified during this storm using MIDAS. Figures 7 and 8 contain TEC maps viewed from the geographic north pole with local noon fixed at the bottom of the map. Figure 7a shows the TEC map of 16:40 UT. A patch visually identified to be located at approximately (72° N, 75° W) is labeled with a black star. The purple contours are LCS ridges

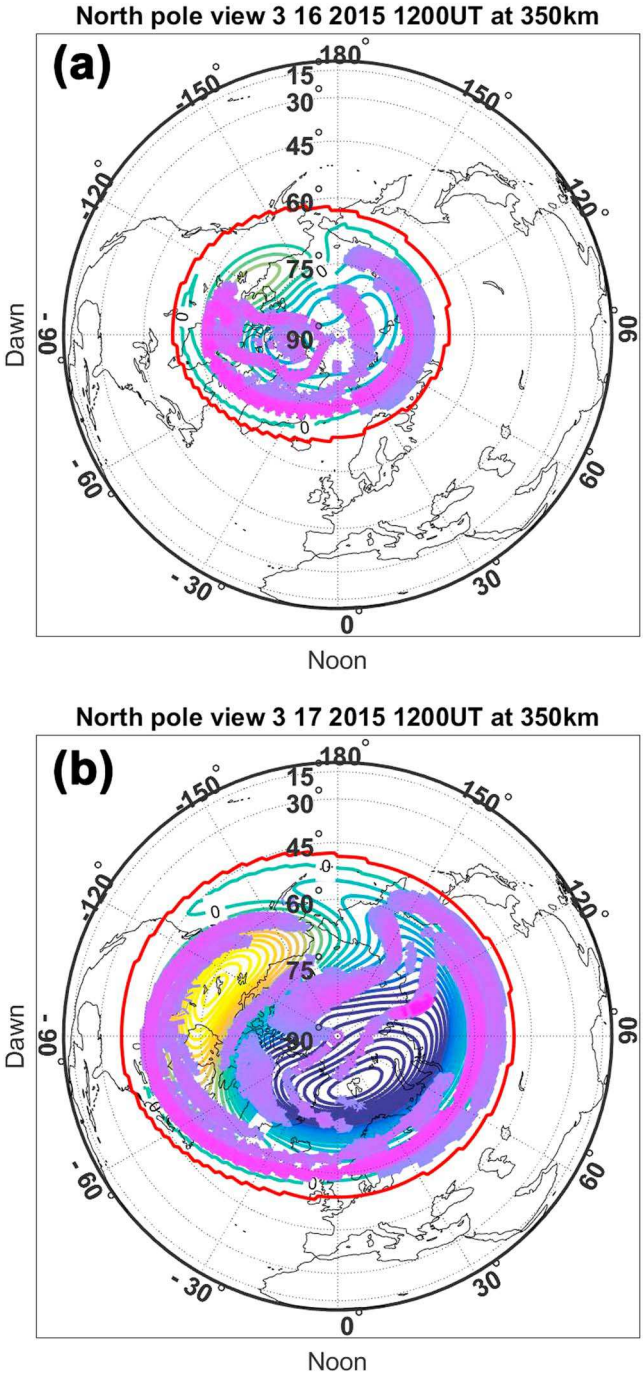

Figure 6. Lagrangian coherent structure ridges (purple) for $\sigma \geq 2.5 \times 10^{-4}$ on the electric potential contours viewed from geographic north pole for (a) geomagnetically quiet period t_0 = 12:00 UT 16 March 2015 and (b) geomagnetically active period t_0 = 12:00 UT 17 March 2015 at 350 km. The red oval is the high latitude electric potential boundary during the interval $t = [t_0, t_f]$.

identified as $\sigma \geq 2.5 \times 10^{-4}$ for t_0= 16:40 UT, 17 March 2015 with τ = 3 hr. Using the Weimer 2005 and IGRF-12 models for convective drift, we trace this patch forward at 20 min intervals over the next 100 min (see Figures 7b–7f), with the current position of the tracer circled in black, and intermediate locations in red dots at 10-minute intervals. These plots span the times at which the MIDAS reconstruction of plasma was independently corroborated by Swarm in situ densities in Figure 3. The Weimer 2005 and IGRF-12 models are providing estimates of drift consistent with TEC observations. This is even in light of the fact that the tracer

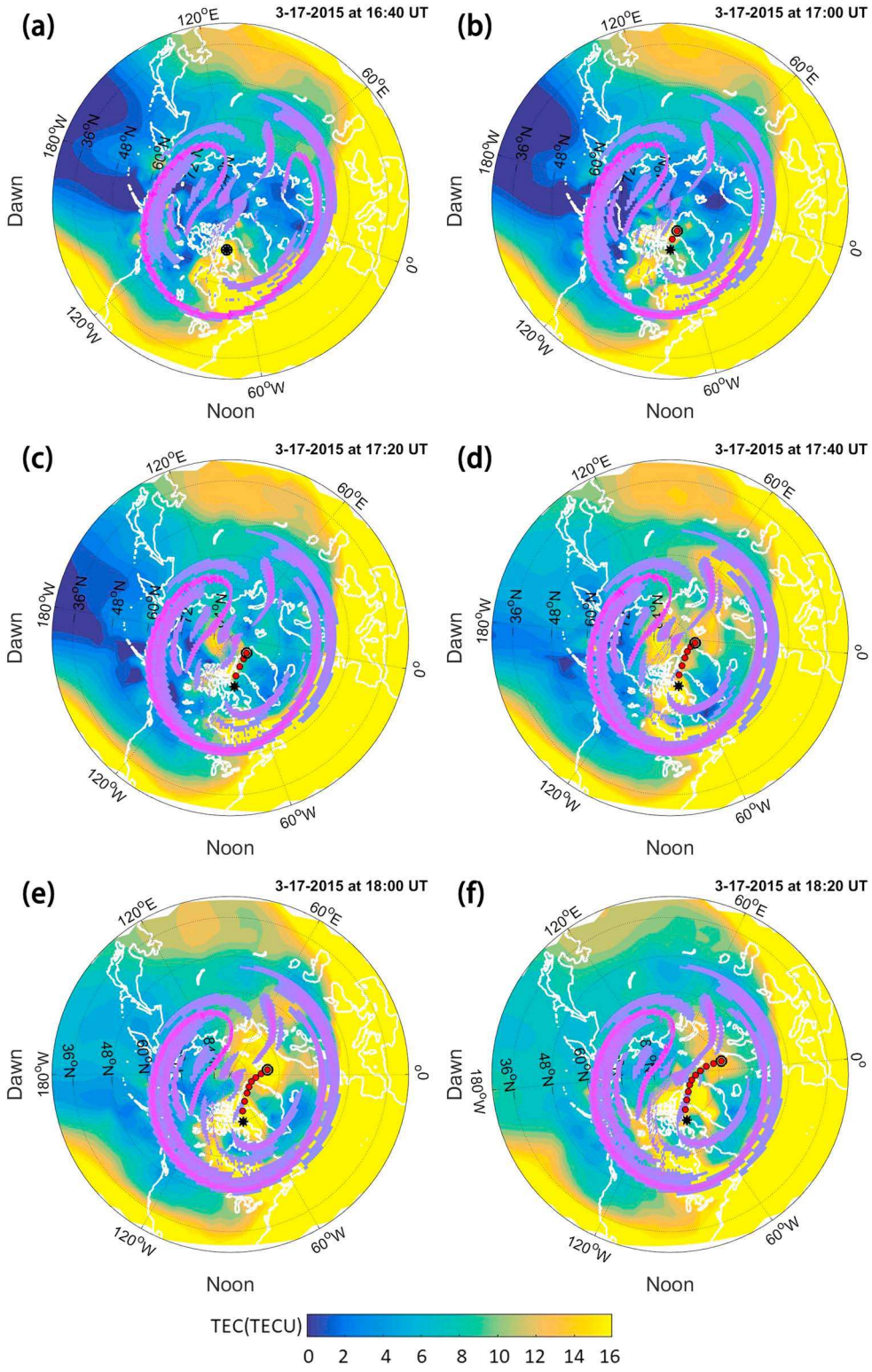

Figure 7. North pole view of total electron content (TEC) maps from MIDAS on 17 March 2015, from 0 to 16 TEC units (TECU), stepping forward in time at 20-min intervals. Local noon is at the bottom of each figure. The purple ridges identify the LCSs of $\sigma \geq 2.5 \times 10^{-4}$ for a given t_0, with $\tau = 3$ hr. A black star represents the initial position (72° N, 75° W) of a polar cap patch identified at 16:40 UT. Modeled tracer locations for the patch are identified with red circles at 10-min intervals. The tracer circled is the position at the current time in each figure. Modeled tracer locations for the patch are identified with red circles at 10-min intervals. (a) 16:40 UT, (b) 17:00 UT, (c) 17:20 UT, (d) 17:40 UT, (e) 18:00 UT, and (f) 18:20 UT. MIDAS = Multi-Instrument Data Analysis System.

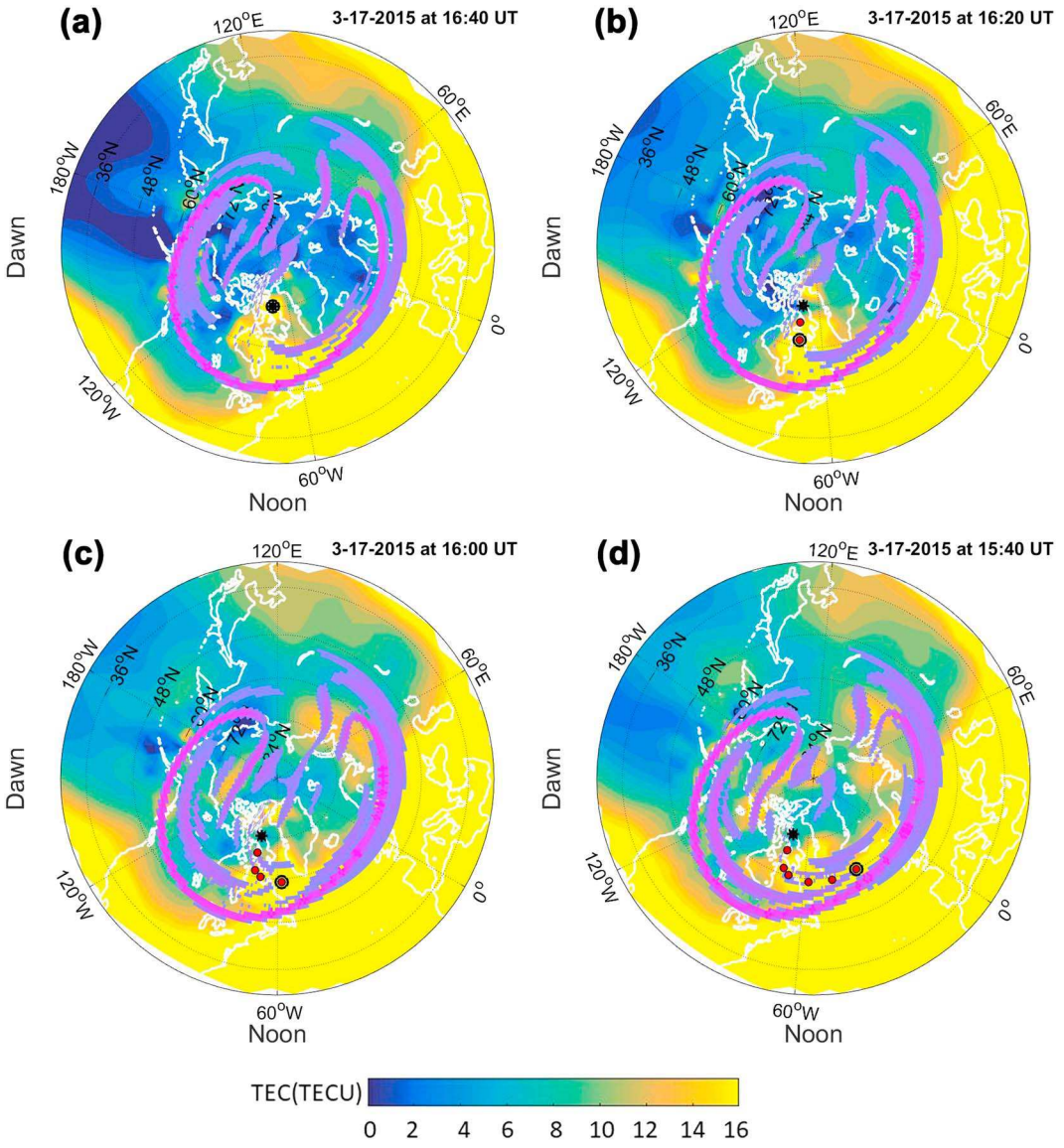

Figure 8. North pole view of total electron content (TEC) maps from MIDAS on 17 March 2015, from 0 to 16 TEC units (TECU) stepping backwards in time at 20-min intervals. Local noon is at the bottom of each figure. The purple ridges identify the LCSs of $\sigma \geq 2.5 \times 10^{-4}$ for a given t_0, with τ = 3 hr. A black star represents the initial position (72° N, 75° W) of a polar cap patch identified at 16:40 UT. Modeled tracer locations for the patch are identified with red circles at 10 min intervals. The tracer circled is the position at the current time in each figure. Modeled tracer locations for the patch are identified with red circles at 10-min intervals. (a) t_0 = 16:40 UT, (b) t_0 = 16:20 UT, (c) t_0 = 16:00 UT, and (d) t_0 = 15:40 UT. MIDAS = Multi-Instrument Data Analysis System.

is assumed to be at 450-km altitude, whereas TEC is a vertically integrated plasma density. This means that the LCSs shown are likely representative of the material transport barriers during this event. These show the modeled LCSs form channels through which the patches propagate.

In Figures 8a–8d, the patch is traced backward in time from 16:40 UT at 20-min intervals over the previous hour. The TEC maps in Figures 8a–8d indicate that the observed patch originated from a tongue of ionization (TOI) extending poleward from a storm enhanced density (SED) at about 60° W longitude. This is to be expected as patches are understood to come from TOIs in the literature.

Figure 8a shows that the center of the patch observed from the MIDAS image is poleward of the LCS ridge at t_0 = 16:40 UT. The TOI throughout the time interval shown (both prior and subsequent to 16:40 UT) also appears to be poleward of the horseshoe LCS for each respective t_0. However, the vast bulk of the SED

is *equatorward* of the LCS. Figures 8a–8d show that the part of the SED poleward of the LCS ridge is the TOI and that therefore it has the potential to become a polar cap patch in the future. In other words, the horseshoe LCS appears to demarcate a necessary condition for the formation of a polar cap patch by the criterion that SED plasma exist poleward of it. When SED plasma is poleward of the LCS, it can be entrained into a polar cap patch. The video in the supporting information animates the LCS ridges for $\sigma \geq 2.5 \times 10^{-4}$, and high-latitude TEC viewed from the geographic north pole for different initial times over the interval t_0 = [10:00 UT, 20:50 UT], $\tau = 3$ hr on 17 March 2015.

5. Discussion

Since convective transport structures in the high-latitude ionosphere map out to the dayside magnetosphere, an important implication of this work is that the LCS ridge in the high latitude ionosphere should map out along field lines to the dayside magnetopause. So the existence of a horseshoe ridge in the ionosphere would demarcate the most highly separating magnetic field lines, which are carried along by the plasma. The horseshoe likely describes those flux tubes which are undergoing the most stretching over the time interval considered. Interestingly, the LCS opening on the nightside shows that there is no significant analogous magnetotail coherent structure, of maximal repulsion. A backward time FTLE calculation would define LCSs of maximal convergence, which are likelier to be on the nightside ionosphere with corresponding locations in the magnetotail.

It may or may not be a coincidence that the LCS we show is similar in shape, though different in orientation, to the horseshoe aurora observed during an IMF southward event during which part of the auroral oval was missing (Tsurutani et al., 1998). In this work we focused on flow transport of plasma. The relationship between the auroral oval, substorms, and LCSs are beyond the scope of this particular study.

Note that in this work, we have examined synoptic scale model convection drifts. This scale of flow field does not include smaller scale turbulent flow velocities, so this work does not address the LCSs that might be produced at regional (100 km or even smaller) scales due to various instability mechanisms. However, to the extent that the TOI and patches are confined to within the channel demarcated by the LCSs and instabilities form on the structure boundaries, the LCSs may provide an approximate location at which instabilities are likelier to form. Such an implication should be examined in the future. The plasma convection in this study is simplified as the high-latitude horizontal $\vec{E} \times \vec{B}$ drift by ignoring other contributions to drift. However, to examine LCSs globally, a study would need to be conducted with modeled plasma drifts including electric Pedersen drift, gravitational Pedersen drift, pure gravitational drift, and parallel mean flow (Atul et al., 2018; Sotnikov et al., 2014). This would likely lead to a three-dimensional flow field, requiring 3-D LCS analysis, which ITALCS does not currently treat.

6. Summary

LCS ridges for plasma drifts in the ionosphere are predicted to exist based on flows simulated with Weimer 2005 and IGRF-12. For the cases studied, the strongly repelling ridges are predominantly horseshoe-like structures centered in the day sector and curving back on themselves to form the opening of a "U" on the nightside. During a geomagnetic storm, LCSs have more complicated topologies and appear at lower latitudes. The strong separation between simulated tracers located on different sides of the LCS ridge illustrates that the LCS location indicates strong stretching. LCS analysis indicates that a necessary condition for the formation and transport of the polar cap patch in ionospheric plasma drifts is that a region of high-density plasma exist poleward of the dayside LCS in order to be entrained into the polar cap.

Since the Weimer 2005 model has an equatorward boundary at which the potential goes to 0, all locations equatorward of this point will have 0 drift velocity. Our study thus makes no claims about LCSs at low latitudes. A simulation including both low- and high-latitude electrodynamics would likely require a full 3-D drift field integration in ITALCS.

Appendix A: Canonical Flow Validation

The double gyre consists of two vortices that alternately expand and contract with time. Figure A1a shows the forward-time FTLE values from 0 (blue) to 5 (yellow) over the double-gyre domain when integrated forward in time from $t_0 = 0$ s with $\tau = 1$ s. The FTLE values quantify the degree of separation, and the LCS is composed

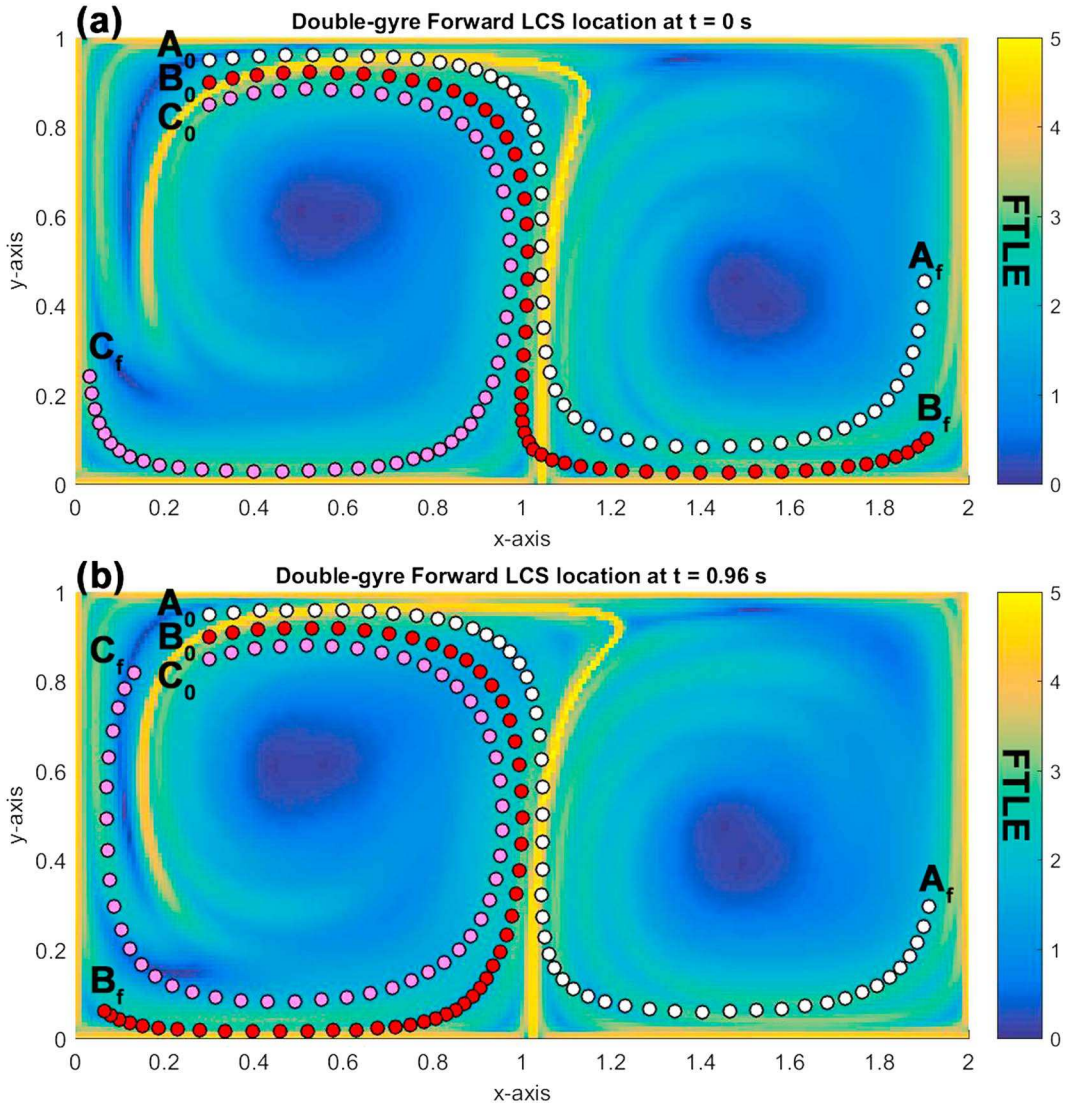

Figure A1. Finite-time Lyapunov exponent (FTLE) map for time-varying double-gyre field for (a) $t_0 = 0$ s. (b) $t_0 = 0.96$ s with the integration time $\tau = 1$ s. The color scale in each map represents the FTLE value ranging from 0 to 5. The three traers' initial and final positions are labeled as A_0 and A_f for white, B_0 and B_f for red, and C_0 and C_f for magenta.

of the locally maximum FTLE values (i.e., the bright yellow curve). The LCS surface indicates the strongest separation of the flow (the most stretching of the fluid element) in the local area. The LCS can be seen running up the center of the domain and curving left toward the top. This is a snapshot of the LCS at time t_0. In a time-varying flow field, the LCS itself advects over time (not shown).

Figure A1a also shows the location of three tracer particles in the double-gyre and their movements over time. There are three equally spaced tracer particles on the plot initially at A_0, B_0, and C_0. Tracers A_0 and B_0 are on the same side of the LCS, while tracers B_0 and C_0 are on opposite sides of the structure. Subsequent locations of the particles are shown for later epochs $t_0 + i\Delta t$ during the integration time. The end locations of particles A and B are A_f and B_f, both to right half of the domain, and particle C_f ends up to the left of it. The particles B_0, C_0 initially straddling the LCS have a larger separation distance $\overline{B_f C_f}$ between their end locations, and thus show a stronger stretching than tracers A and B, which began on the same side of the LCS.

In addition, the LCS for a different start time even with same time interval τ has different initial conditions so is not the same LCS (Haller, 2015). Figure A1b shows the LCS of the double gyre for initial time $t_0 = 0.96$ s, $\tau = 1$ s. The shape of the structure can be seen running up the center of the domain and curving right then left toward the top. Because the flow map yields a different LCS for $t_0 = 0.96$ s than for $t_0 = 0$ s, the particles

starting at identical initial locations A_0, B_0, and C_0 to Figure A1a, but at a different moment in time, undergo different stretching. Here the particles starting at A_0 and B_0 end up further apart than B_0 and C_0 do.

As shown in Figure A1 for the time-varying double-gyre flow field, different initial conditions yield different LCS ridges. In Figures A1a and A1b, the FTLE maps are a snapshot of LCSs at two different values of t_0 while the tracers are plotted at regular intervals within $t = [t_0, t_0 + \tau]$. For this reason tracer trajectories appear to cross the LCS ridges. In addition, using data assimilation drifts from methods such as Estimating Model Parameters from Ionospheric Reverse Engineering (EMPIRE; Miladinovich et al., 2016) and Super Dual Auroral Radar Network (SuperDARN; Ruohoniemi et al., 1989) could provide data-driven plasma drifts that could be used as the inputs to ITALCS in the future.

Appendix B: Velocity Transformation

For the $\vec{E} \times \vec{B}$ drift model, the velocity of each gridpoint will be described as a linear velocity ground speed, but the LCS grid is parameterized by angles $(x^1 = \phi, x^2 = \lambda)$. For these reasons, the velocity is transformed to angular rates $\dot{\phi}$, $\dot{\lambda}$ as described below.

Figure B1 shows a diagram of the relevant frames and coordinate systems on a sphere of radius r. earth-centered, earth-fixed (ECEF) frame E has coordinates $\hat{e}_1, \hat{e}_2, \hat{e}_3$ and origin O. A Lagrangian frame L is at point P and moves with a particle that is at point P at time t. The L frame's coordinates $\hat{l}_1, \hat{l}_2, \hat{l}_3$ are locally up-east-north, respectively. The angles $\phi = \phi_0 + \Delta\phi$, $\lambda = \lambda_0 + \Delta\lambda$ are the longitude and latitude of a particle at point P with $\Delta\phi_0 = \Delta\lambda_0 = 0$ at time t_0 and ϕ_0 and λ_0 are constant. The position of particle P from O is

$$\vec{r}^P = r\hat{l}_1 \tag{B1}$$

where $r = R_E + h$, a summation of the mean radius of Earth (R_E) and the height (h) of a certain atmospheric layer, is constant. Kinematically, the velocity of particle P in the ECEF frame is the time derivative of $\vec{r}^P$:

$${}^E\vec{v}^P = \frac{{}^E d\vec{r}^P}{dt} \tag{B2}$$

$$= \frac{{}^L d\vec{r}^P}{dt} + {}^E\vec{\omega}^L \times \vec{r}^P \tag{B3}$$

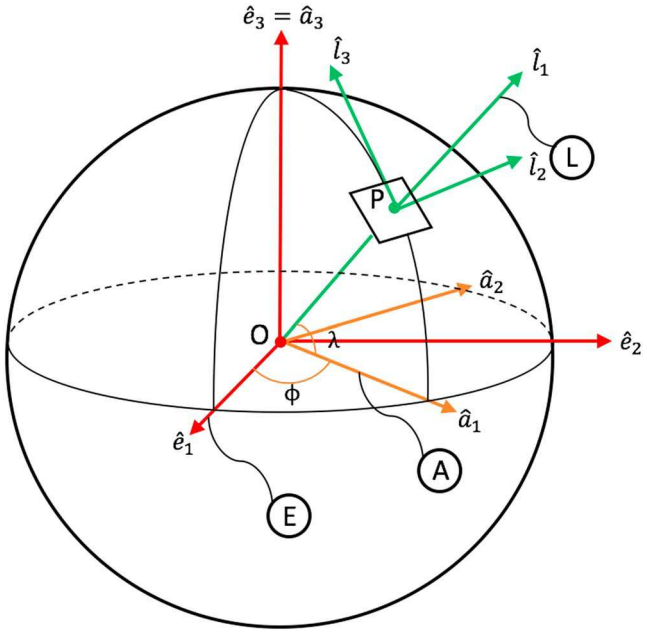

Figure B1. Relationship between ECEF frame and Lagrangian frame. ECEF = earth-centered, earth-fixed.

where the presuperscript indicates the observer's frame. The time derivative of $\vec{r}^P$ as seen in the L frame differs from that seen in the E frame due to the angular velocity ${}^E\vec{\omega}^L$ that observer E sees the L frame having. Because the position $\vec{r}^P$ is constant in the L frame, $\frac{{}^L d\vec{r}^P}{dt} = 0$, so the first term in Equation (B3) vanishes, leaving

$$ {}^E\vec{v}^P = {}^E\vec{\omega}^L \times \vec{r}^P \tag{B4}$$

There are two rotations between the E and L frames. The first rotation is from the E frame to an intermediate frame A about the $\hat{e}_3$ axis with the rate $\dot{\phi}$. The second rotation is from frame A to frame L about the $-\hat{I}_2$ axis with the rate $\dot{\lambda}$, which gives

$$ {}^E\vec{\omega}^L = {}^E\vec{\omega}^A + {}^A\vec{\omega}^L \tag{B5}$$

$$ = \dot{\phi}\hat{a}_3 - \dot{\lambda}\hat{I}_2 \tag{B6}$$

$$ = \dot{\phi}\left(\cos\lambda\hat{I}_3 + \sin\lambda\hat{I}_1\right) - \dot{\lambda}\hat{I}_2 \tag{B7}$$

Substitute equations (B7) and (B1) into equation (B4)

$$ {}^E\vec{v}^P = \dot{\phi}r\cos\lambda\hat{I}_2 + \dot{\lambda}r\hat{I}_3 \tag{B8}$$

The horizontal velocity of the particle at point P as seen in the ECEF frame is provided as

$$ {}^E\vec{v}^P = v_e\hat{I}_2 + v_n\hat{I}_3 \tag{B9}$$

where v_e and v_n are the eastward and northward components, respectively. Comparing equation (B8) with equation (B9) then we have

$$ \dot{\phi} = \frac{v_e}{r\cos\lambda} \tag{B10}$$

$$ \dot{\lambda} = \frac{v_n}{r} \tag{B11}$$

Equations (B10) and (B11) form the velocity field that are time-integrated in ITALCS to search for LCSs globally.

Since the spherical domain mesh is over longitude and latitude, the closed non-Euclidean domain is periodic in both longitude and latitude. This periodicity requires additional logic in ITALCS to keep particles within a longitudinal domain of $(\phi_{min}, \phi_{max}) = (-180°, 180°)$ and latitude domain of $(\lambda_{min}, \lambda_{max}) = (-90°, 90°)$. To convert the longitude and latitude of gridpoints flowing "beyond" the boundaries to their locations within the domain, the coordinates need to be wrapped around back into the domain. Figure B2 shows three map projections of the global domain meshed by longitude ϕ and latitude λ.

Figure B2a illustrates the boundary problem caused by the longitude limit on an azimuthal orthographic projection of the world with $\phi = \pm 180°$ as the central meridian. When a particle $P_{(lon)i}$ travels westward across the longitude line $\phi = -180°$, it should arrive at $P_{(lon)i+1}$. However, given the regularly gridded configuration space (ϕ, λ) shown in Figure B2c, the particle $P_{(lon)i}$, located at time t_i, traveling westward across the west boundary $\phi = -180°$, will exit the domain stopping at $P'_{(lon)i+1}$. In order to ensure the domain remains closed, the missing point must be brought back to its equivalent location within the domain to $P_{(lon)i+1}$. As shown in Figure B2c, when the particle $P_{(lon)i}$ runs out of the leftmost boundary, it will return from the rightmost boundary, and vice versa. Based on this, $\vec{r}^{P_{lon}} = (\phi_{P_{lon}}, \lambda_{P_{lon}})$ can be updated as

$$ \lambda_{P_{lon}} = \lambda'_{P_{lon}} \tag{B12}$$

$$ \phi_{P_{lon}} = ((\phi'_{P_{lon}} - \phi_{min}) \mod (\phi_{max} - \phi_{min})) + \phi_{min} \tag{B13}$$

where $\phi_{max} = 180°, \phi_{min} = -180°$. This logic works for windings of more than 360°. After updating the coordinate, particle P will remain within the longitudinal domain.

Figures B2b and B2c show the boundary problem caused by the latitude limit. Figure B2b shows a general perspective projection view of the north pole. As shown in Figure B2b, when the particle $P_{(lat)i}$ travels across the north pole, it must end at $P_{(lat)i+1}$ and remain in the domain. However, the single north pole point corresponds to the entire top boundary of the domain as shown in Figure B2c. For particle $P_{(lat)i}$ to travel across

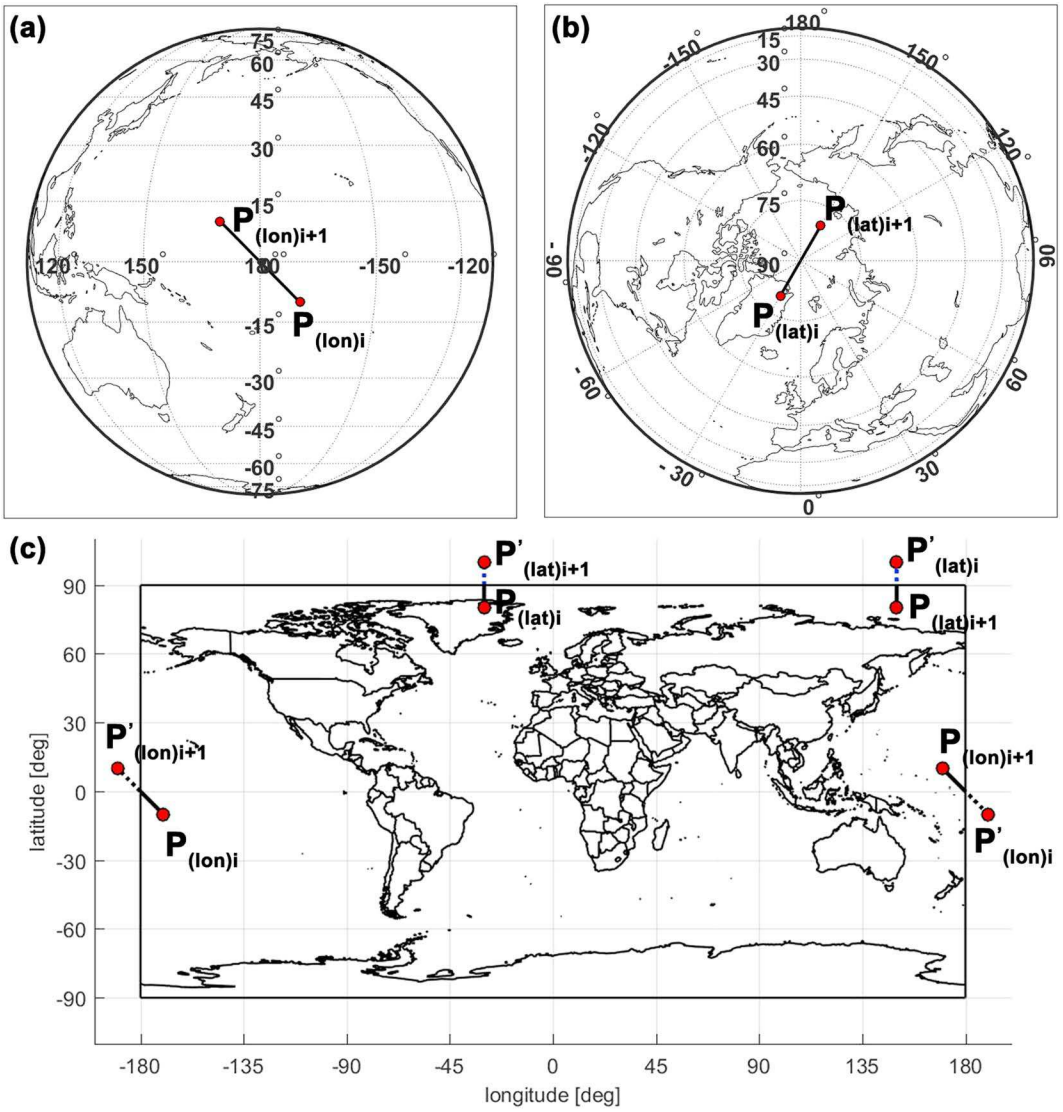

Figure B2. (a) Longitude boundary-crossing illustration: general perspective projection viewed of the world with $\phi = \pm 180°$ as the central meridian. (b) Latitude boundary-crossing illustration: general perspective projection viewed of the world from north pole; (c) geographic projection, which corresponds to a regular spacing of our generalized coordinates ϕ, λ.

the north pole it must go due north to cross the $\lambda = 90°$ boundary. In order to keep the domain closed, the position of $\vec{r}^{P}_{lat} = (\phi_{P_{lat}}, \lambda_{P_{lat}})$ needs to be updated as

$$a = \left\lfloor \frac{\lambda'_{P_{lat}} - \lambda_{min}}{\lambda_{max} - \lambda_{min}} \right\rfloor \tag{B14}$$

$$\lambda_{P_{lat}} = 180(a \mod 2) + (-1)^a (\lambda'_{P_{lat}} \mod 360) \tag{B15}$$

$$\phi_{P_{lat}} = \phi'_{P_{lat}} - \mathrm{sgn}\phi'_{P_{lat}} (180) \times (a \mod 2) \tag{B16}$$

where $\lambda_{max} = 90°, \lambda_{min} = -90°$, and the symbol $\lfloor \rfloor$ represents the floor operation. These expressions are generalizations of the $|\lambda| < 180°$ case, for which λ is changed to the supplementary angle, and ϕ is shifted by 180°. Both latitude and longitude domain crossings are generalized because velocities near the poles can become near-singular and could produce ϕ, λ more than one winding beyond the domain. These boundary crossings are checked and updated at each step of integration.

Acknowledgments
This work was supported by the National Science Foundation AGS-1352602 and the Armour College of Engineering Program for Undergraduate Research Education (PURE) award. Alex Chartier acknowledges support from NSF grant OPP-1643773. The authors thank the reviewers and Editors for their insightful and constructive comments. The authors thank Daniel Weimer for the electric potential model source code. Weimer model results are also available at the Community Coordinated Modeling Center (https://ccmc.gsfc.nasa.gov/models/modelinfo.php?model=Weimer). The AE index values are available at the World Data Center (WDC) for Geomagnetism, Kyoto for AE index service, and the Multi-Instrument Data Analysis System (MIDAS) input data can be retrieved from the International GNSS Service (http://www.igs.org/products). The 12th generation International Geomagnetic Reference Field (IGRF-12) model is available at International Union of Geodesy and Geophysics (https://www.ngdc.noaa.gov/IAGA/vmod/igrf.html). Swarm data can be retrieved from European Space Agency (https://earth.esa.int/web/guest/swarm/data-access) through the ftp://swarm-diss.eo.esa.int/ portal. MIDAS TEC results, Weimer 2005 model outputs, IGRF-12 outputs, and ITALCS outputs shown in the paper may be obtained by contacting the authors.

References

Anderson, D. N., Decker, D. T., & Valladares, C. E. (1996a). Global Theoretical Ionospheric Model (GTIM). In R. W. Schunk (Ed.), *Solar-terrestrial energy program: Handbook of ionospheric models* (pp. 133–152). Logan UT: Center for Atmospheric and Space Sciences.

Anderson, D. N., Decker, D. T., & Valladares, C. E. (1996b). Modeling boundary blobs using time varying convection. *Geophysical Research Letters*, *23*(5), 579–582. https://doi.org/10.1029/96GL00371

Atul, J. K., Singh, R., Sarkar, S., Kravchenko, O. V., Singh, S. K., Chattopadhyaya, P. K., & Kaw, P. K. (2018). Magnetic shear damped polar convective fluid instabilities. *Journal of Geophysical Research: Space Physics*, *123*, 808–818. https://doi.org/10.1002/2017JA024778

BozorgMagham, A., Ross, S., & Schmale, D. (2013). Real-time prediction of atmospheric lagrangian coherent structures based on forecast data: an application and error analysis. *Physica D: Nonlinear Phenomena*, *258*, 47–60. https://doi.org/10.1016/j.physd.2013.05.003

Burston, R., Mitchell, C., & Astin, I. (2016). Polar cap plasma patch primary linear instability growth rates compared. *Journal of Geophysical Research: Space Physics*, *121*, 3439–3451. https://doi.org/10.1002/2015JA021895

Bust, G. S., & Crowley, G. (2007). Tracking of polar cap ionospheric patches using data assimilation. *Journal of Geophysical Research*, *112*, A05307. https://doi.org/10.1029/2005JA011597

Bust, G. S., & Mitchell, C. N. (2008). History, current state, and future directions of ionospheric imaging. *Reviews of Geophysics*, *46*, RG1003. https://doi.org/10.1029/2006RG000212

Carlson, H. C. (2012). Sharpening our thinking about polar cap ionospheric patch morphology, research, and mitigation techniques. *Radio Science*, *47*, RS0L21. https://doi.org/10.1029/2011RS004946

Chartier, A. T., Mitchell, C. N., & Jackson, D. R. (2012). A 12 year comparison of MIDAS and IRI 2007 ionospheric Total Electron Content. *Advances in Space Research*, *49*(9), 1348–1355. https://doi.org/10.1016/j.asr.2012.02.014

Crowley, G. (1996). Critical review of ionospheric patches and blobs. *The Review of Radio Science*, *1993-1996*, 619–648.

Datta-Barua, S., Su, Y., Deshpande, K., Miladinovich, D., Bust, G. S., Hampton, D., & Crowley, G. (2015). First light from a kilometer-baseline Scintillation Auroral GPS Array. *Geophysical Research Letters*, *42*, 3639–3646. https://doi.org/10.1002/2015GL063556

Decker, D. T., Valladares, C. E., Sheehan, R., Basu, S., Anderson, D. N., & Heelis, R. A. (1994). Modeling daytime F layer patches over Sondrestrom. *Radio Science*, *29*(1), 249–268. https://doi.org/10.1029/93RS02866

du Toit, P. C., & Marsden, J. E. (2010). Horseshoes in hurricanes. *Journal of Fixed Point Theory and Applications*, *7*(2), 351–384. https://doi.org/10.1007/s11784-010-0028-6

Foster, J. C. (1993). Storm time plasma transport at middle and high latitudes. *Journal of Geophysical Research*, *98*(A2), 1675–1689. https://doi.org/10.1029/92JA02032

Foster, J. C., Coster, A. J., Erickson, P. J., Holt, J. M., Lind, F. D., Rideout, W., et al. (2005). Multiradar observations of the polar tongue of ionization. *Journal of Geophysical Research*, *110*, A09S31. https://doi.org/10.1029/2004JA010928

Grigoriev, R. O. (Ed.) (2011). *Transport and mixing in laminar flows: From microfluidics to oceanic currents*. Weinheim, Germany: John Wiley. https://doi.org/10.1002/9783527639748

Haller, G. (2005). An objective definition of a vortex. *Journal of Fluid Mechanics*, *525*, 1–26. https://doi.org/10.1017/S0022112004002526

Haller, G. (2015). Lagrangian coherent structures. *Annual Review of Fluid Mechanics*, *47*, 137–162. https://doi.org/10.1146/annurev-fluid-010313-141322

Hosokawa, K., St-Maurice, J. P., Sofko, G. J., Shiokawa, K., Otsuka, Y., & Ogawa, T. (2010). Reorganization of polar cap patches through shears in the background plasma convection. *Journal of Geophysical Research*, *115*, A01303. https://doi.org/10.1029/2009JA014599

Hosokawa, K., Tsugawa, T., Shiokawa, K., Otsuka, Y., Nishitani, N., Ogawa, T., & Hairston, M. R. (2010). Dynamic temporal evolution of polar cap tongue of ionization during magnetic storm. *Journal of Geophysical Research*, *115*, A12333. https://doi.org/10.1029/2010JA015848

Hosokawa, K., Tsugawa, T., Shiokawa, K., Otsuka, Y., Ogawa, T., & Hairston, M. R. (2009). Unusually elongated, bright airglow plume in the polar cap F region: Is it a tongue of ionization? *Geophysical Research Letters*, *36*, L07103. https://doi.org/10.1029/2009GL037512

Hunsucker, R. D., & Hargreaves, J. K. (2003). *The high-latitude ionosphere and its effects on radio propagation*. Cambridge, UK: Cambridge University Press.

Kamide, Y., & Rostoker, G. (2004). What is the physical meaning of the AE index? *Eos, Transactions American Geophysical Union*, *85*(19), 188–192. https://doi.org/10.1029/2004EO190010

Kirchengast, G. (1996). The Graz ionospheric flux tube simulation model. In R. W. Schunk (Ed.), *Solar-terrestrial Energy program: Handbook of ionospheric models* (pp. 73–94). Logan UT: Center for Atmospheric and Space Sciences.

Le, G., Lühr, H., Anderson, B. J., Strangeway, R. J., Russell, C. T., Singer, H., et al. (2016). Magnetopause erosion during the 17 March 2015 magnetic storm: Combined field-aligned currents, auroral oval, and magnetopause observations. *Geophysical Research Letters*, *43*, 2396–2404. https://doi.org/10.1002/2016GL068257

Lockwood, M., & Carlson, H. C. (1992). Production of polar cap electron density patches by transient magnetopause reconnection. *Geophysical Research Letters*, *19*(17), 1731–1734. https://doi.org/10.1029/92GL01993

Lockwood, M., Davies, J. A., Moen, J., van Eyken, A. P., Oksavik, K., McCrea, I. W., & Lester, M. (2005). Motion of the dayside polar cap boundary during substorm cycles: II. Generation of poleward-moving events and polar cap patches by pulses in the magnetopause reconnection rate. *Annales Geophysicae*, *23*(11), 3513–3532. https://doi.org/10.5194/angeo-23-3513-2005

MacDougall, J., & Jayachandran, P. T. (2007). Polar patches: Auroral zone precipitation effects. *Journal of Geophysical Research*, *112*, A05312. https://doi.org/10.1029/2006JA011930

Miladinovich, D. S., Datta-Barua, S., Bust, G. S., & Makela, J. J. (2016). Assimilation of thermospheric measurements for ionosphere-thermosphere state estimation. *Radio Science*, *51*, 1818–1837. https://doi.org/10.1002/2016RS006098

Mitchell, C. N., & Spencer, P. S. (2003). A three-dimensional time-dependent algorithm for ionospheric imaging using GPS. *Annals of Geophysics*, *46*(4), 687–696. https://doi.org/10.4401/ag-4373

Moen, J., Hosokawa, K., Gulbrandsen, N., & Clausen, L. B. N. (2015). On the symmetry of ionospheric polar cap patch exits around magnetic midnight. *Journal of Geophysical Research: Space Physics*, *120*, 7785–7797. https://doi.org/10.1002/2014JA020914

Moen, J., Oksavik, K., Alfonsi, L., Daabakk, Y., Romano, V., & Spogli, L. (2013). Space weather challenges of the polar cap ionosphere. *Journal of Space Weather and Space Climate*, *3*, A02. https://doi.org/10.1051/swsc/2013025

Oksavik, K., Barth, V. L., Moen, J., & Lester, M. (2010). On the entry and transit of high-density plasma across the polar cap. *Journal of Geophysical Research*, *115*, A12308. https://doi.org/10.1029/2010JA015817

Peacock, T., & Haller, G. (2013). Lagrangian coherent structures: The hidden skeleton of fluid flows. *Physics Today*, *66*(2), 41. https://doi.org/10.1063/PT.3.1886

Ruohoniemi, J. M., Greenwald, R. A., Baker, K. B., Villain, J.-P., Hanuise, C., & Kelly, J. (1989). Mapping high-latitude plasma convection with coherent HF radars. *Journal of Geophysical Research*, *94*(A10), 13,463–13,477. https://doi.org/10.1029/JA094iA10p13463

Shadden, S. C., Lekien, F., & Marsden, J. E. (2005). Definition and properties of Lagrangian coherent structures from finite-time Lyapunov exponents in two-dimensional aperiodic flows. *Physica D: Nonlinear Phenomena*, *212*(3-4), 271–304. https://doi.org/10.1016/j.physd.2005.10.007

Sojka, J. J., Bowline, M. D., Schunk, R. W., Decker, D. T., Valladares, C. E., Sheehan, R., et al. (1993). Modeling Polar Cap F-Region Patches Using Time Varying Convection. *Geophysical Research Letters*, *20*(17), 1783–1786. https://doi.org/10.1029/93GL01347

Sotnikov, V., Kim, T., Lundberg, J., Paraschiv, I., & Mehlhorn, T. A. (2014). Scattering of electromagnetic waves by vortex density structures associated with interchange instability: Analytical and large scale plasma simulation results. *Physics of Plasmas*, *21*(5), 052309. https://doi.org/10.1063/1.4879021

Spencer, P. S. J., & Mitchell, C. N. (2007). Imaging of fast moving electron-density structures in the polar cap. *Annals of Geophysics*, *50*(3), 427–434. https://doi.org/10.4401/ag-3074

Tang, W., & Mahalov, A. (2013). Stochastic Lagrangian dynamics for charged flows in the E-F regions of ionosphere. *Physics of Plasmas*, *20*(3), 032305. https://doi.org/10.1063/1.4794735

Thébault, E., Finlay, C. C., Beggan, C. D., Alken, P., Aubert, J., Barrois, O., et al. (2015). International Geomagnetic Reference Field: the 12th generation. *Earth Planets and Space*, *67*, 1–19. https://doi.org/10.1186/s40623-015-0228-9

Tsurutani, B. T., Arballo, J. K., Lakhina, G. S., Ho, C. M., Ajello, J., Pickett, J. S., et al. (1998). The January 10, 1997 auroral hot spot, horseshoe aurora and first substorm: A CME loop? *Geophysical Research Letters*, *25*(15), 3047–3050. https://doi.org/10.1029/98GL01304

Venditti, J. G., Hardy, R. J., Church, M., & Best, J. L. (2013). What is a coherent flow structure in geophysical flow? In J. G. Venditti, et al. (Eds.), *Coherent flow structures at Earth's surface* (Chap. 1, pp. 402). Chichester, UK: Wiley Blackwell.

Wang, N., Ramirez, U., Flores, F., & Datta-Barua, S. (2017). Lagrangian coherent structures in the thermosphere: Predictive transport barriers. *Geophysical Research Letters*, *44*, 4549–4557. https://doi.org/10.1002/2017GL072568

Weber, E. J., Buchau, J., Moore, J. G., Sharber, J. R., Livingston, R. C., Winningham, J. D., & Reinisch, B. W. (1984). F layer ionization patches in the polar cap. *Journal of Geophysical Research*, *89*(A3), 1683–1694. https://doi.org/10.1029/JA089iA03p01683

Weimer, D. R. (2005). Predicting surface geomagnetic variations using ionospheric electrodynamic models. *Journal of Geophysical Research*, *110*, A12307. https://doi.org/10.1029/2005JA011270

Zhang, Q. H., Zhang, B. C., Liu, R. Y., Dunlop, M. W., Lockwood, M., Moen, J., et al. (2011). On the importance of interplanetary magnetic field $|B_y|$ on polar cap patch formation. *Journal of Geophysical Research*, *116*, A05308. https://doi.org/10.1029/2010JA016287

Zhang, Q.-H., Zhang, B.-C., Lockwood, M., Hu, H.-Q., Moen, J., Ruohoniemi, J. M., et al. (2013). Direct observations of the evolution of polar cap ionization patches. *Science*, *339*(6127), 1597–1600. https://doi.org/10.1126/science.1231487

Zhang, Q. H., Zhang, B. C., Moen, J., Lockwood, M., McCrea, I. W., Yang, H. G., et al. (2013). Polar cap patch segmentation of the tongue of ionization in the morning convection cell. *Geophysical Research Letters*, *40*, 2918–2922. https://doi.org/10.1002/grl.50616

Zou, S., Moldwin, M. B., Ridley, A. J., Nicolls, M. J., Coster, A. J., Thomas, E. G., & Ruohoniemi, J. M. (2014). On the generation/decay of the storm-enhanced density plumes: Role of the convection flow and field-aligned ion flow cell. *Journal of Geophysical Research: Space Physics*, *119*, 8543–8559. https://doi.org/10.1002/2014JA020408